OPEN ACCESS

Visualizing cell–cell communication using synthetic notch activated MRI

TianDuo Wang[a,b], Yuanxin Chen[b], Nivin N. Nystrom[a,b], Shirley Liu[a,b], Yanghao Fu[a,b], Francisco M. Martinez[a], Timothy J. Scholl[a,b,c], and John A. Ronald[a,b,d,e,f,1]

Cell–cell communication plays a fundamental role in multicellular organisms. Cell-based cancer immunotherapies rely on the ability of innate or engineered receptors on immune cells to engage specific antigens on cancer cells to induce tumor kill. To improve the development and translation of these therapies, imaging tools capable of noninvasively and spatiotemporally visualizing immune-cancer cell interactions would be highly valuable. Using the synthetic Notch (SynNotch) system, we engineered T cells that upon interaction with a chosen antigen (CD19) on neighboring cancer cells induce the expression of optical reporter genes and the human-derived, magnetic resonance imaging (MRI) reporter gene organic anion transporting polypeptide 1B3 (OATP1B3). Administration of engineered T cells induced the antigen-dependent expression of all our reporter genes in mice bearing CD19-positive tumors but not CD19-negative tumors. Notably, due to the high spatial resolution and tomographic nature of MRI, contrast-enhanced foci within CD19-positive tumors representing OATP1B3-expressing T cells were clearly visible and their distribution was readily mapped. We then extended this technology onto human natural killer-92 (NK-92) cells, observing similar CD19-dependent reporter activity in tumor-bearing mice. Furthermore, we show that when delivered intravenously, engineered NK-92 cells can be detected via bioluminescence imaging in a systemic cancer model. With continued work, this highly modular imaging strategy could aid in the monitoring of cell therapies in patients and, beyond this, augment our understanding of how different cell populations interact within the body during normal physiology or disease.

cell–cell communication | cell therapy | MRI | reporter gene | synthetic Notch

The ability for cells to sense their local environment and properly communicate with neighboring cells plays a fundamental role in multicellular organisms during development, homeostasis, and pathogenesis. Cell–cell communication is largely mediated through the presence of various receptors and ligands, and these interactions have been leveraged to develop cell-based therapies, revolutionizing treatment approaches for infectious and neurological diseases, autoimmune disorders, and cancer (1, 2).

Some of the most promising cell therapies include a plethora of cell-based cancer immunotherapies such as tumor infiltrating lymphocytes (TILs), T cell receptor T (TCR-T) cells, and most notably, chimeric antigen receptor T (CAR-T) cells (3–5). These strategies harness the remarkable ability of immune cells to patrol the body and interact with cancer cells via endogenous or engineered receptors to elicit cytotoxic effects (6, 7). While these therapies have demonstrated transformative results for treating certain malignancies, they can have on-target, off-tumor activities that induce life-threatening side effects and may also fail at producing complete or sustained cancer remission in some patients (8, 9). Without a solid understanding of where and how these cells interact with healthy and malignant tissues, it is difficult to understand why these therapies result in poor efficacy and/or serious adverse events in individual patients. Technologies that can visualize the fate of these cells after infusion, particularly their antigen-specific communication with neighboring cells, would lead to improvements in both the safety and efficacy of these therapies during their development and clinical translation.

Clinical methods to monitor cellular immunotherapies include biopsies or blood tests (10), which fail to provide spatial information on the therapeutic activity of cells, especially in the context of multi-organ metastatic disease. Noninvasive and clinically relevant imaging technologies such as positron emission tomography (PET) and magnetic resonance imaging (MRI), that can spatiotemporally monitor immune cells in vivo, would be advantageous for preclinical research, clinical trials, and potentially routine clinical care. MRI is highly attractive due to its widespread clinical use and ability to generate highly resolved three-dimensional images with anatomical information and excellent soft tissue contrast.

Significance

Adoptive immune cell therapies have shown remarkable clinical success for the treatment of certain blood-based cancers, with potential for other cancer types on the horizon. However, these treatments are not effective in some patients and/or induce serious side effects in others. A better understanding of where these therapeutic cells go and how they interact in the body is key for addressing these challenges. In this study, we demonstrate a novel bioengineering strategy in immune cells that allows antigen-dependent, cell–cell communication to be visualized within tumors in mice using optical and MRI. We posit these tools will improve our ability to monitor cell therapies in patients using established clinical imaging modalities and promote the development of novel cell-based products.

However, conventional MRI is not easily able to track cells after adoptive transfer without any labeling strategy. One labeling strategy involves pre-loading therapeutic cells with magnetic resonance (MR)-visible nanoparticles prior to infusion (11); however, this approach is limited to short-term monitoring of viable cells. An alternative approach that facilitates long-term monitoring is engineering cells to express reporter genes that encode proteins that can be detected by imaging (12–14). The ideal reporter gene for cell tracking would pair a human-compatible gene and a clinically used imaging probe.

The organic anion transporting polypeptide 1 (OATP1) family of transporters has been previously established as a positive-contrast MRI reporter for cell tracking (15, 16). Our group and others have demonstrated the liver-derived human OATP1B3 isoform can readily take up the clinically approved contrast agent gadolinium ethoxybenzyl diethylenetriamine pentaacetic acid (Gd-EOB-DTPA; Trade name: Primovist/Eovist), and this reporter system has been used to track the location and growth of engineered cancer cells in mouse models (17–19). Excitingly, we recently demonstrated that OATP1B3-MRI can be used to visualize metastatic tumors composed of as few as ~1,000 cells (20). Due to the high sensitivity of OATP1B3-MRI cell tracking, we posited it may be useful for in vivo monitoring of cell-based immunotherapies, particularly their antigen-specific communication with cancer cells—the prerequisite of tumor cytotoxicity occurring within the immunological synapse. Thus far, optical microscopy techniques have allowed direct cell–cell communication to be imaged in cell culture and small animals (7, 21–26). Although some of these studies have shed light onto the mechanisms within the immunological synapse, they are limited to small fields-of-view and are not readily translatable to humans. Therefore, we aimed to create a more ideal imaging strategy by developing a synthetic biology system that triggers OATP1B3 expression in an activatable manner to allow the detection of immune-cancer interactions with whole-body MRI (27).

Inspired by the Notch signaling pathway, the synthetic Notch (SynNotch) system was first described in 2016 as a versatile cellular gene circuit which allows for transcriptional manipulation in response to unique environmental inputs (28). The system is composed of a chimeric SynNotch receptor with an extracellular antigen-sensing domain, Notch regulatory core, and intracellular effector domain. Receptor-ligand binding leads to proteolytic cleavage, freeing the effector transcriptional activator domain, and allowing it to dissociate into the nucleus to modulate the expression of desired transgenes encoded in a SynNotch response element. SynNotch gene circuits have been used to detect cell–cell interactions via fluorescence, control cellular functions in T cells, create morphogen gradients to control tissue development, drive gene editing, and bolster CAR-T therapy to better target solid tumors (29–36). Here, we leveraged SynNotch to drive antigen-dependent expression of the OATP1B3 reporter for MRI, as well as optical reporter genes for fluorescence imaging (FLI) and bioluminescence imaging (BLI) to facilitate multimodal preclinical imaging. We engineered immune cells with SynNotch receptors directed against the B cell surface antigen CD19, a well-established target for CAR-T cell therapies in the clinic (37, 38). We demonstrate that SynNotch-antigen interactions induced expression of multimodal reporter genes and showcase optical imaging and MRI of cell–cell communication in mice.

Results

Engineering of T Cells with a SynNotch Reporter Imaging System.
We designed an activatable reporter imaging system for integration into immune cells, in which engagement of SynNotch receptor with CD19 induces the expression of tdTomato (tdT) for FLI, firefly luciferase (FLuc) for BLI, and organic anion transporting polypeptide 1B3 (OATP1B3) for MRI (Fig. 1 A and B). Naïve human Jurkat T cells were sequentially transduced first with the response element (RE) encoding these reporter genes to generate "RE only" T cells, then an anti-CD19 SynNotch receptor to generate "SynNotch+RE" T cells which contained the fully functional gene circuit (39). To boost the expression of SynNotch and/or RE components to levels comparable to other studies (28), T cells were twice transduced with each component to create final populations of cells used in this study unless otherwise stated (Fig. 1C). To confirm that our engineering did not drastically alter the phenotype of the cells, flow cytometry was used to analyze
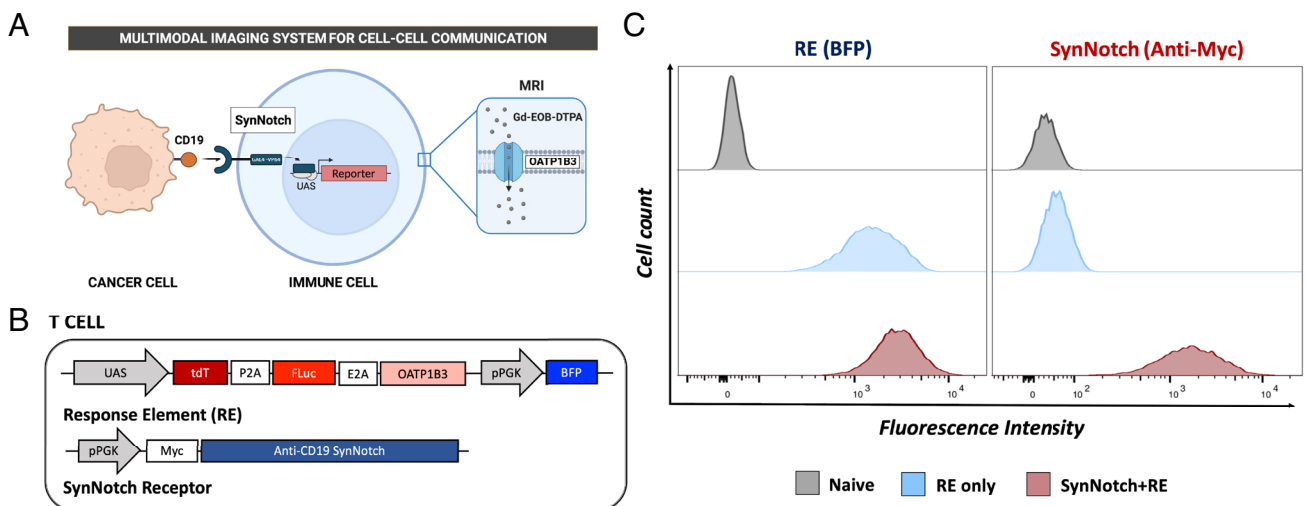

Fig. 1. Engineering of T cells with multimodal imaging system for cell–cell communication. (A) Schematic of SynNotch system. CD19 binding by SynNotch receptor induces intracellular cleavage of a GAL4-VP64 transactivator, which binds to an UAS containing 5× GAL4 DNA-binding domains 5′ to a minimal CMV promoter to initiate transcription of encoded reporter genes. For MRI, OATP1B3 transgene is encoded which is a transporter that can take up the contrast agent Gd-EOB-DTPA. (B) Vector map of human Jurkat T cells transduced with a response element (RE) encoding tdT, FLuc, and OATP1B3, well as a pPGK-driven BFP for sorting. Cells were then engineered with a pPGK-driven, CD19-targeting SynNotch receptor which was Myc-tagged for sorting. (C) Flow cytometry of naïve and engineered T cells post-sorting to assess expression of RE (BFP+) and SynNotch (Myc+).

common T cell surface markers (*SI Appendix,* Fig. S1*A*). Among the three populations, similar percentages of cells displayed T cell receptor (TCR), CD3, CD4, and CD8 at the cell surface, although some small differences in CD3 and CD4 were observed ($P < 0.05$), which may be owned to differences in cell health and staining. The proliferation rates of naïve and engineered T cell were assessed, and the relative growth rates of cell populations over 24 and 48 h were not significantly ($P > 0.41$) different from each other (*SI Appendix,* Fig. S1*B*).

Cell–Cell Interactions Induce Reporter Gene Expression in an Antigen-Dependent Manner in T Cells. To validate our SynNotch imaging system in vitro, SynNotch+RE T cells were co-cultured with naïve Nalm6 leukemia cells which endogenously express the B cell antigen CD19. Visualizing the dynamics of reporter activation using fluorescence microscopy, tdT signal can be first

detected roughly 8 h following co-culturing of cells and the maximum number of tdT-positive cells was detected between 24 and 32 h (Fig. 2*A*). Thus, we determined that co-culturing cells for 24 h would be a suitable time point to detect reporter gene activation moving forward. To control for antigen-independent reporter activation, we knocked out CD19 from Nalm6 cells to generate CD19-negative target cells (Fig. 2*B*). When naïve or RE only T cells were co-cultured with Nalm6 cells at a 1:1 ratio for 24 h, <0.2% of T cells were positive for tdT and these values were the same between co-cultures with CD19+ and CD19– Nalm6 cells (Fig. 2*C*). Contrastingly, ~22.5% of SynNotch+RE T cells co-cultured with CD19+ cells exhibited tdT expression, while ~2.9% tdT was detectable in CD19– co-cultures. Similarly, BLI was used to assess FLuc reporter activation 24 h after co-culturing at a 1:1 ratio (Fig. 2*D*). Naïve and RE only T cells exhibited minimal BLI signal, which did not significantly differ between
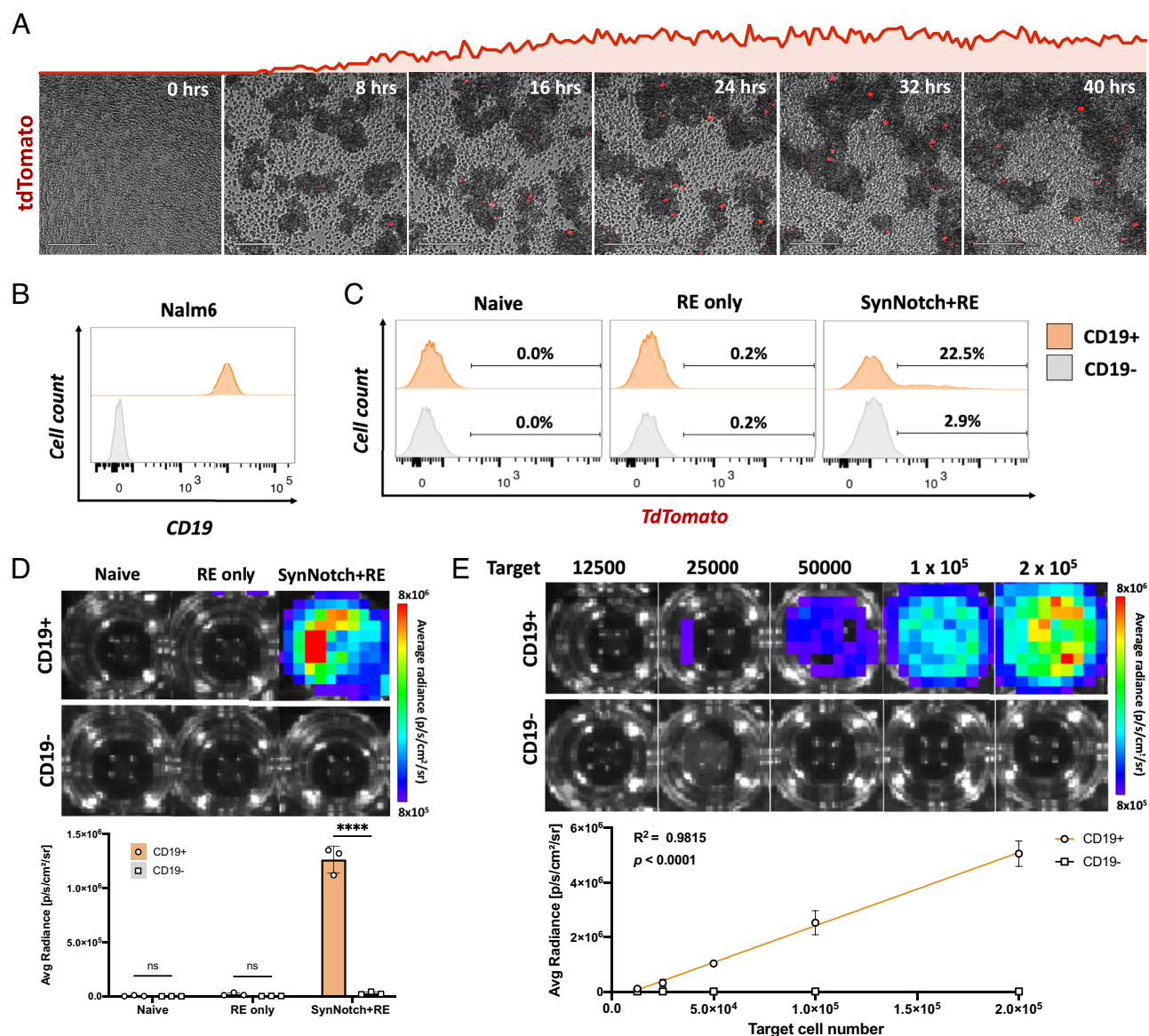

Fig. 2. In vitro assessment of SynNotch reporter system in T cells. (*A*) Fluorescence microscopy with brightfield overlay visualizing tdT expression in SynNotch+RE T cells following co-culturing with CD19+ Nalm6 cells at a 1:1 ratio over a 40 h time period. The object count of tdT+ cells is shown above images. (Scale bar, 200 μm.) (*B*) Flow cytometry measuring CD19 expression in CD19+ and CD19− Nalm6 cells. (*C*) Flow cytometry measuring tdT expression in T cells 24 h after co-culturing with CD19+ or CD19− Nalm6 cells at a 1:1 ratio. (*D*) FLuc BLI in T cells 24 h after co-culturing with CD19+ or CD19− Nalm6 cells at a 1:1 ratio and quantification (N = 3). (*E*) FLuc BLI at 24 h after co-culturing with varying number of Nalm6 cells and quantification (N = 3). Data are presented as mean ± SD (****$P < 0.0001$, ns, not significant).

CD19+ and CD19− co-cultures ($P > 0.99$). In contrast, BLI signal was significantly higher in SynNotch+RE T cells when co-cultured with CD19+ cells versus CD19− cells ($P < 0.0001$). To evaluate how varying the number of target cells would impact reporter gene activation, co-cultures were repeated by changing Nalm6 cell numbers added to each well (Fig. 2E). In CD19+ co-cultures, BLI signal showed a significant positive correlation to target cell number ($R^2 = 0.9815$, $P < 0.0001$), whereas for CD19− co-cultures, BLI signal remained at baseline levels and was not influenced by target cell number ($R^2 = 0.0126$, $P > 0.69$). To validate that OATP1B3 was active within reporter-expressing cells, we performed an uptake assay with the fluorescent Live/Dead Fixable Green (LDG) Dye, which normally has low permeability in live cells, but has been previously shown to be a substrate transported by OATP1B3 (40). We found significantly higher uptake of LDG when SynNotch+RE T cells were co-cultured with CD19+ cells versus CD19− cells, indicative of higher OATP1B3 activity in the presence of CD19 (*SI Appendix*, Fig. S2A, $P < 0.0001$). Moreover, to assess potential toxicities from cellular uptake of Gd-EOB-DTPA, CD19+ co-cultures were incubated with various concentrations of Gd-EOB-DTPA. We observed no significant differences between the viability of SynNotch+RE T cells without any agent and T cells incubated with Gd-EOB-DTPA doses as high as 16 mM (*SI Appendix*, Fig. S2B, $P > 0.05$).

Bioluminescence Imaging Reveals Antigen-Dependent Activation of Luciferase in Mice. As the first in vivo evaluation of our SynNotch imaging system, we established subcutaneous tumors on the flanks of immunocompromised mice using either CD19+ or CD19− Nalm6 cells. Once tumors became palpable and were ~150 mm^3, SynNotch+RE T cells were injected intratumorally and BLI was performed over time to visualize FLuc activity (Fig. 3A). As a pilot, we used SynNotch+RE T cells which were transduced only once, we observed elevated FLuc signal in CD19+ compared to CD19− tumors at all time points post-cell injection, however no significant difference was found likely due to a small sample size ($P > 0.06$) (*SI Appendix*, Fig. S3). A second set of experiments was performed using SynNotch+RE T cells that were transduced and sorted twice. As expected, minimal BLI signal was detected in mice carrying CD19+ and CD19− Nalm6 tumors prior to cell injection with no significant differences ($P > 0.97$) (Fig. 3 B and C and *SI Appendix*, Fig. S2A). As early as 12 h post-cell injection, mice carrying CD19+ tumors showed significantly elevated BLI signal compared to mice with CD19− tumors ($P < 0.01$). BLI signal peaked around 24 h post-cell injection, which was consistent with our findings in vitro and was significantly higher in CD19+ versus CD19− tumors at 24 h ($P < 0.001$) and at all time points afterward. It is possible that a small, but non-significant, increase in BLI signal seen in CD19− tumors at 12 h post-cell injection might be pointing to a small amount of leakiness for expression of FLuc; however, more data would need to be gathered to understand this result. These findings further supported an imaging time point of roughly 24 h post-intratumoral injection of engineered T cells would be optimal for detecting antigen-dependent reporter activation which maximizes signal-to-background.

MRI Reveals Localized Contrast-Enhanced Foci within Tumors that Signal Cell–Cell Communication. Considering the high sensitivity of BLI compared to MRI, we were motivated to visualize antigen-dependent immune-cancer interactions using MR reporter imaging. Twenty-four hours following intratumoral injection of SynNotch+RE T cells, T_1-weighted MRI was performed pre- and post-administration with Gd-EOB-DTPA contrast agent (Fig. 4A). Pre-contrast images revealed that both CD19+ and CD19− tumors appeared to be vastly homogenous
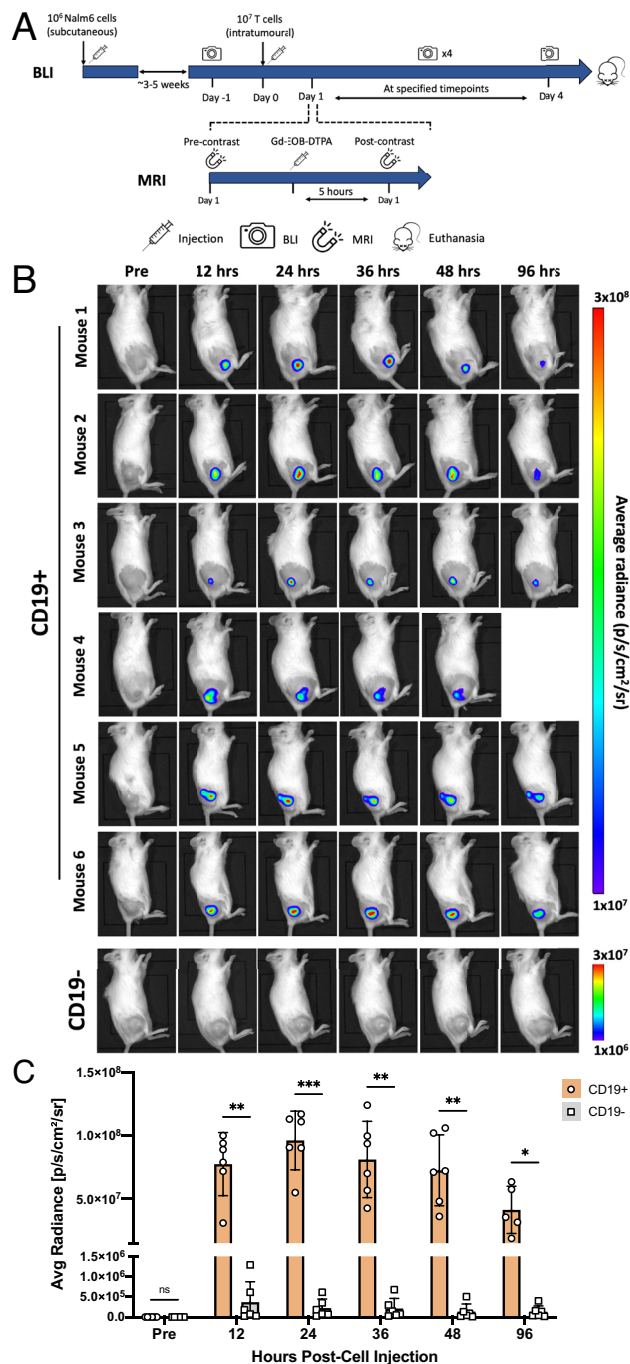

Fig. 3. Bioluminescence imaging of antigen-dependent luciferase activation in mice. (A) Experimental timeline for subcutaneous tumor inoculation, T cell injection, and reporter gene imaging. (B) FLuc BLI in mice with subcutaneous CD19+ or CD19− Nalm6 tumors pre- and post-intratumoral injection with SynNotch+RE T cells with (C) quantification (N = 6). Images for remaining mice in CD19− group can be found in *SI Appendix*, Fig. S4. Data are presented as mean ± SD (***$P < 0.001$, **$P < 0.01$, *$P < 0.05$, ns, not significant).

with no obvious contrast enhancement. Post-contrast MRI was performed 5 h following administration of Gd-EOB-DTPA to allow non-specific uptake in tissues to clear, and we observed no regions of remarkable contrast enhancement in CD19− tumors (Fig. 4A and *SI Appendix*, Fig. S2B). Contrastingly, in post-contrast images of CD19+ tumors, we observed clear regions of contrast enhancement across all six mice. To better represent the spatial distribution of enhanced foci across the entire tumor, for every transverse MRI slice, we generated intensity profiles which mapped the pixel gray values along a straight line drawn
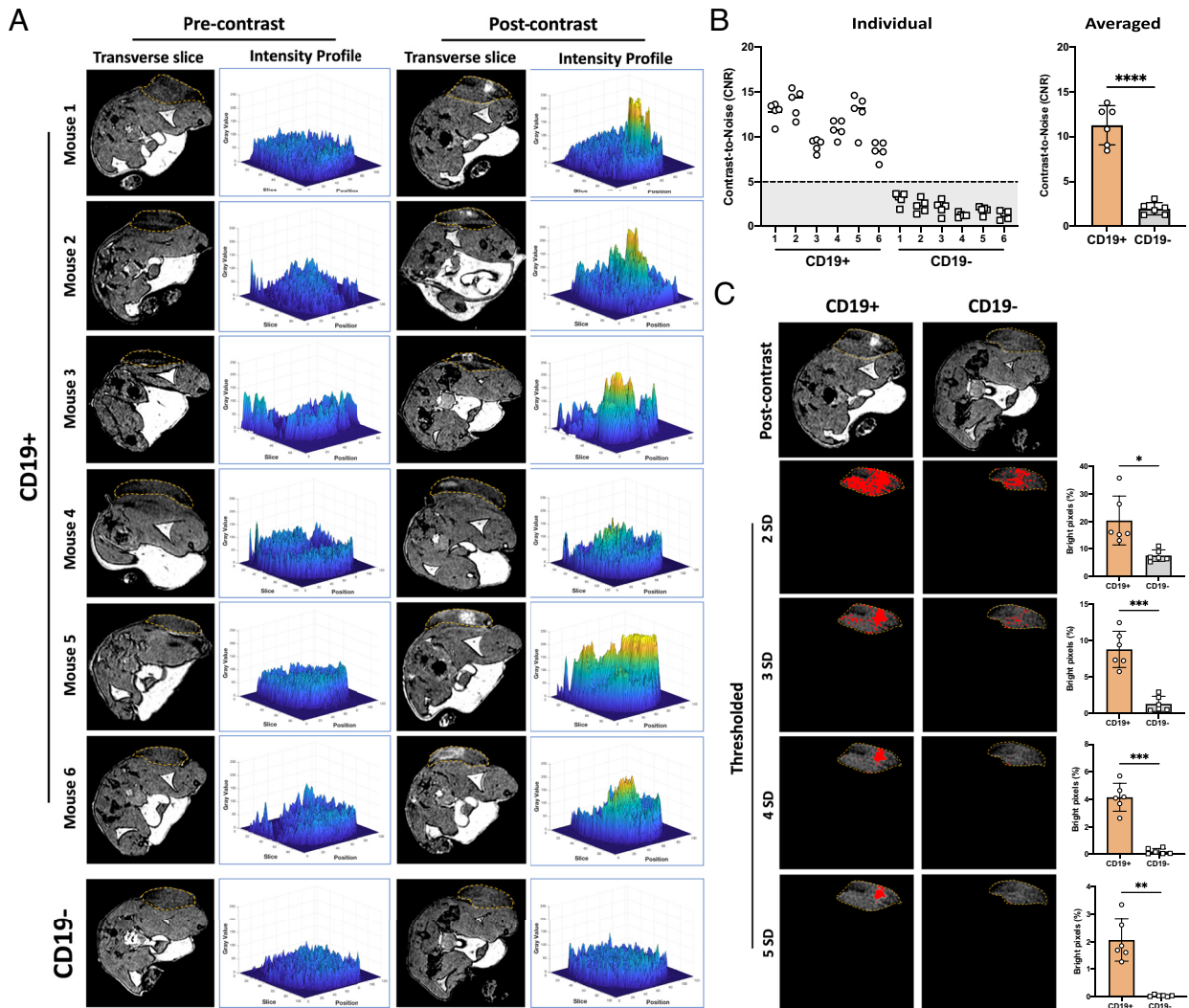
Fig. 4. Contrast-enhanced MRI of cell–cell communication in mice. (*A*) T$_1$-weighted MR images acquired pre- and 5 h post-contrast with Gd-EOB-DTPA. Tumors are outlined in yellow on representative transverse slices. Intensity profiles map pixel "gray value" across a straight line "position" drawn through each tumor for every transverse "slice." Images for remaining mice in CD19− group can be found in *SI Appendix*, Fig. S4. (*B*) CNR of enhanced regions compared to tumor background calculated on individual slices (five slices per mouse) and averaged per mouse (N = 6). (*C*) Representative manual segmentations and thresholding of post-contrast tumors to identify bright pixels (red). Pixels are considered bright if above intensity thresholds determined as mean +2SD, +3SD, +4SD, and +5SD from corresponding pre-contrast images for each mouse. The percentage of bright pixels is calculated by dividing the number of bright pixels by the total number of pixels over the entire tumor volume (right graphs; N = 6). Data are presented as mean ± SD (****P < 0.0001, ***P < 0.001, **P < 0.01, *P < 0.05).

through the middle of the tumor (Fig. 4*A*). Intensity profiles for CD19− tumors remained mainly homogeneous and with minimal differences in profiles from pre- and post-contrast images. For CD19+ tumors, intensity profiles between pre-contrast images were also mainly homogeneous; however, profiles from post-contrast images displayed regions of high pixel intensity. The distribution and intensity of enhanced regions in CD19+ varied between animals, owing to inherent variability in intratumoral delivery. Contrast-to-noise ratio (CNR) of enhanced tumor regions compared to tumor background (non-enhanced tumor area) on individual slices through each tumor was determined by a blinded observer. CNR values for individual slices through each tumor ranged between 7 and 15 for CD19+ tumors, whereas CNR values from CD19− tumors were all below five (Fig. 4*B*). The average CNR values were significantly higher for CD19+ tumors (11.28 ± 2.36) than CD19− tumors (1.96 ± 0.84, P < 0.0001). Additionally, to compare contrast differences between groups throughout the entire tumor volume, the number of "bright" pixels across each tumor post-contrast was quantified by identifying pixels above a threshold calculated from corresponding pre-contrast images for each mouse. Post-contrast

CD19+ tumors displayed a significantly higher percentage of bright tumor pixels than CD19− tumors across all thresholds (Fig. 4*C*, P < 0.05). Qualitatively, on images with thresholding applied, using thresholds of mean pre-contrast tumor intensity plus three or four SDs (mean + 3SD or mean + 4SD) identified enhanced regions on post-contrast images most similarly to our blinded observer.

Histological Analyses of Tumors Identify Regions with Reporter-Expressing Cells. Histology on subcutaneous tumors was performed at endpoint and assessed using fluorescence microscopy. No obvious tdT fluorescence was observed across the entire CD19− tumor section, matching the lack of contrast-enhanced regions detected by MRI and low BLI signal (Fig. 5*A*). For CD19+ tumors, the areas of tdT fluorescence across the tumor section corresponded well with the contrast-enhanced foci observed on manually matched MRI slices. At a higher magnification, we observed tdT fluorescence and OATP1B3 immunostaining fluorescence in CD19+ tumors, but not CD19− tumors, supporting antigen-specific reporter activation in intratumoral T cells (Fig. 5*B*). Moreover, the areas of tdT and
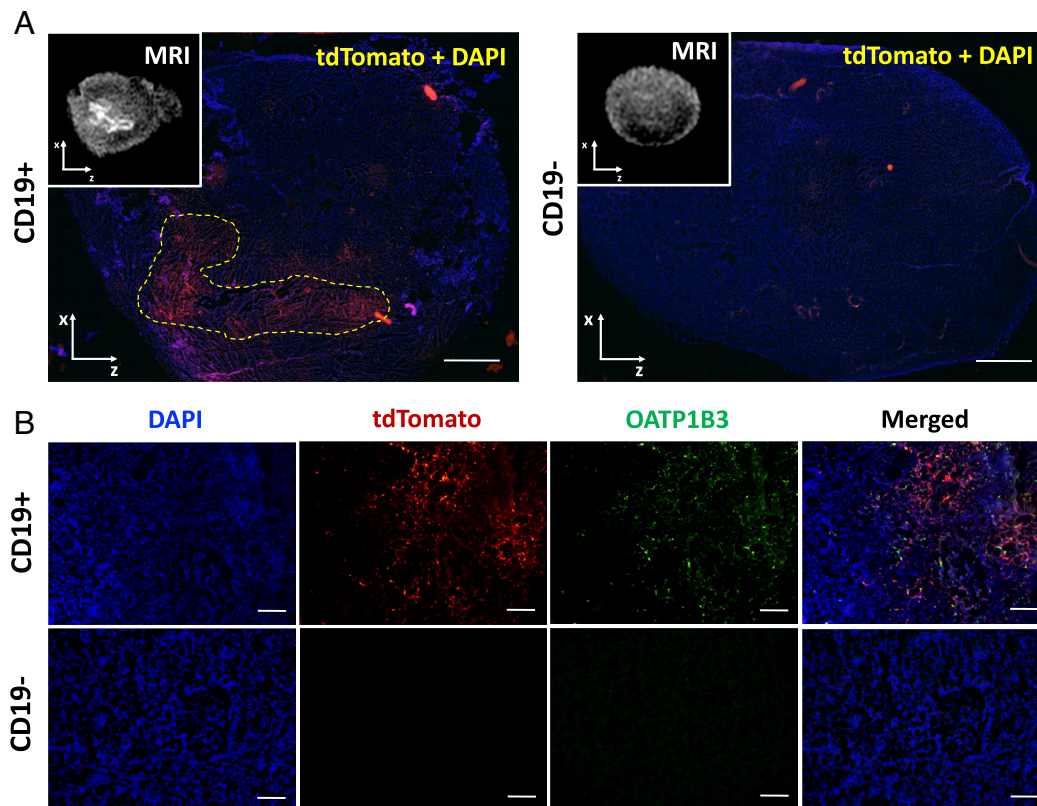
Fig. 5. Endpoint tumor histology to visualize reporter-expressing cells. (*A*) Fluorescence microscopy of tdT and DAPI counterstaining for a representative whole sagittal tumor section. *Inset* is a representative corresponding sagittal MRI slice for each tumor. For histology and MRI images, *x* axis points in the ventral direction and *z* axis points in the posterior direction (toward mouse tail). Yellow outline indicates regions with tdT fluorescence. (Scale bar, 1 mm.) (*B*) Fluorescence microscopy (10× magnification) of Nalm6 tumors with DAPI, tdT, OATP1B3 immunostaining, and merged images. (Scale bar, 100 μm.)

OATP1B3 fluorescence had high degrees of spatial correspondence qualitatively, indicating T cells expressing both reporters. Lastly, we noted that DAPI counterstaining revealed that CD19+ and CD19– Nalm6 tumors displayed a similarly diffuse tumor architecture with increased extracellular volume.

SynNotch Reporter Imaging System Can Be Adapted to Human Natural Killer Cells. To explore whether our activatable reporter imaging system is adaptable to other immune cell types, we chose to engineer human natural killer-92 (NK-92) cells, a cell line which has already been utilized in patients as a promising adoptive cell therapy (41, 42). Using the same sequential transduction strategy as with T cells, we generated RE only and SynNotch+RE NK cells (*SI Appendix*, Fig. S5 *A* and *B*). We then confirmed that engineering NK cells did not significantly alter proliferation rates compared to naïve counterparts (*SI Appendix*, Fig. S5C). Since NK cells naturally exhibit the ability to kill malignant cells, we investigated whether SynNotch engineering would alter the therapeutic capabilities of our NK-92 cells. When naïve and RE only NK cells were co-cultured with CD19+ Nalm6 cells constitutively expressing a zsGreen fluorescence protein, there were similar levels of killing at various E:T ratios (*SI Appendix*, Fig. S5D). In contrast, SynNotch+RE NK cells displayed significantly greater cancer killing at all E:T ratios compared to naïve and RE only cells ($P < 0.001$), suggesting the antigen-binding SynNotch receptor may boost killing. To assess antigen-dependent reporter activation, NK cells were co-cultured with either CD19+ or CD19– Nalm6 cells at a 1:1 ratio. Roughly 14.4% of SynNotch+RE NKs cells exhibited tdT expression when co-cultured with CD19+ cells, whereas tdT expression for these same NK cells was <1% in CD19– co-culture and <2%

for naïve or RE only NK cells. FLuc signal was minimal in naïve and RE only NK cell co-cultures ($P > 0.05$), whereas FLuc signal was significantly higher in SynNotch+RE NK cells when co-cultured with CD19+ cells (*SI Appendix*, Fig. S6B, $P < 0.0001$). Additionally, FLuc activity was positively related to the number of CD19+, but not CD19-, target cells, although unlike with T cells, BLI output saturated at higher target cell numbers (*SI Appendix*, Fig. S6C, $R^2 = 0.8853$).

For in vivo evaluation, we performed BLI on mice with subcutaneous Nalm6 tumors following intratumoral injection with SynNotch+RE NK cells. As with our T cells, FLuc activity was significantly higher in CD19+ versus CD19– tumors at soon as 12 h post-injection ($P < 0.05$) and peaked at 24 h post-injection (Fig. 6A, $P < 0.001$). In a second cohort of mice with subcutaneous tumors, we aimed to investigate the detection limit of NK cells via MRI by varying the number of NK cells injected intratumorally into each CD19+ tumor (Fig. 6B). No remarkable contrast was found in any tumors pre-contrast or in CD19– tumors post-contrast. In post-contrast MRI of CD19+ tumors and their corresponding intensity profiles, we observed clear regions of contrast enhancement. As the number of NK cells was increased, so did the observed contrast, area of enhancement on intensity profiles, and CNR. Irrespective to the number of NK cells injected, average CNR values for enhanced regions to tumor background were significantly higher for CD19+ tumors than CD19– tumors (Fig. 6C, $P < 0.05$), with CNR for CD19+ tumors ranging between 5 and 10 meanwhile CNR for CD19– tumors was all below five.

Upon validating antigen-specific reporter activation in NK cells in vivo, we then evaluated the ability of our engineered NK cells to home to and induce reporter expression at cancer sites
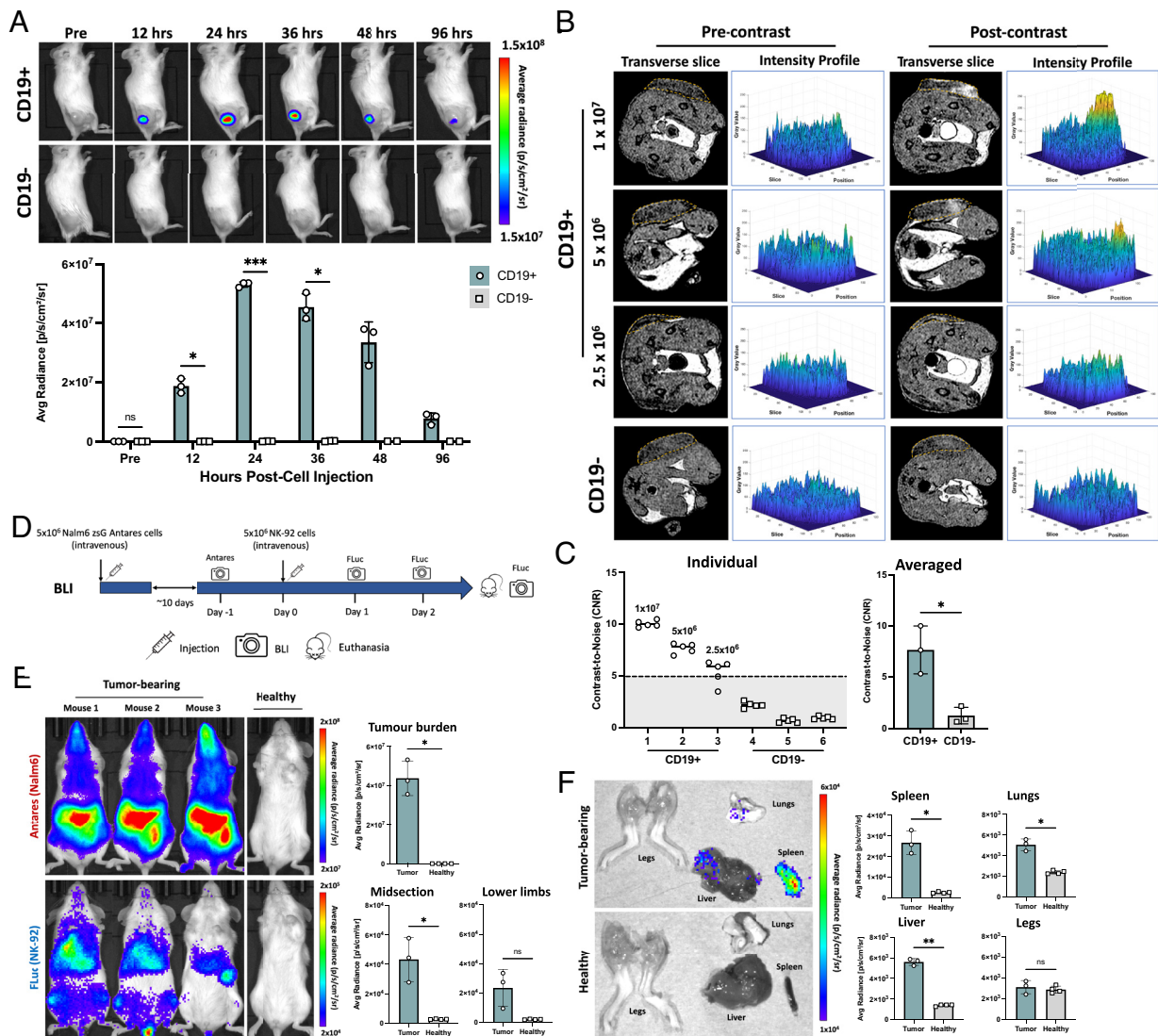
Fig. 6. Adapting multimodal imaging system onto human natural killer-92 (NK-92) cells. Human NK-92 cells were engineered with the same SynNotch gene circuit as with T cells, shown in *SI Appendix*, Fig. S5. (*A*) FLuc BLI in mice with subcutaneous CD19+ or CD19− Nalm6 tumors pre- and post-intratumoral injection with SynNotch+RE NK cells with quantification (N = 3). Images for remaining mice in each group can be found in *SI Appendix*, Fig. S7. (*B*) T_1-weighted MR images acquired pre- and 5 h post-contrast with Gd-EOB-DTPA. Tumors are outlined in yellow on representative transverse slices. Intensity profiles map pixel "gray value" across a straight line "position" drawn through each tumor for every transverse "slice". Images for remaining mice in CD19− group can be found in *SI Appendix*, Fig. S7. (*C*) CNR of enhanced regions compared to tumor background calculated on individual slices (five slices per mouse) and averaged per mouse (N = 3). (*D*) Experimental timeline for intravenous tumor inoculation, NK-92 cell injection, and imaging. (*E*) (*Top*) Antares BLI in mice on day 11 following systemic injection of Antares-expressing Nalm6 cells with quantification, (*Bottom*) FLuc BLI in mice 24 h post-systemic injection with SynNotch+RE NK cells with quantification of signal in midsection and lower limbs (tumor-bearing: N = 3; healthy: N = 4). Images for remaining mice can be found in *SI Appendix*, Fig. S9. (*F*) FLuc BLI of excised organs 48 h post-injection of NK cells with quantification (tumor-bearing: N = 3; healthy: N = 4). Data are presented as mean ± SD (***$P < 0.001$, **$P < 0.01$, *$P < 0.05$, ns, not significant).

when injected intravenously. As done previously, NK-92 cells were irradiated prior to injection to prevent uncontrolled in vivo cell proliferation (43). In a preliminary test, we found that intravenously injected SynNotch+RE NK cells failed to yield detectable BLI signal in subcutaneous Nalm6 tumors (*SI Appendix*, Fig. S8). This may have been due to low persistence and/or homing of irradiated NK cells, and so we hypothesized that shifting to a more relevant systemic leukemia model may allow intravenously delivered NK cells to contact targeted cancer cells more readily. Naïve CD19+ Nalm6 cells were engineered to express the BLI reporter Antares, an orthogonal BLI reporter to FLuc, to track cancer cell growth in mice. Following their intravenous injection, Nalm6 Antares cells were allowed to grow for 11 d, at which Antares BLI signal (i.e., tumor burden) was significantly higher compared to healthy mice (Fig. 6 *D* and *E*). SynNotch+RE

NK cells were then delivered intravenously, and at 24 h post-injection, BLI revealed FLuc was near undetectable in healthy mice, whereas in tumor-bearing mice, FLuc signal was significantly higher in the midsection of tumor-bearing mice compared to healthy mice ($P < 0.05$), and there was an elevated, but non-significant ($P > 0.09$) FLuc signal in the lower limbs (Fig. 6*E* and *SI Appendix*, Fig. S9*A*). By day 2 post-injection, FLuc signal decreased ~threefold from day 1, although the signal was still significantly higher in tumor-bearing mice compared to healthy mice ($P < 0.05$, *SI Appendix*, Fig. S9*B*). Following the imaging session on day 2, mice were sacrificed and ex vivo BLI was performed to locate signal more precisely. We detected significantly greater FLuc signal in the spleen, liver, and lungs, but not the legs, of tumor-bearing versus healthy mice ($P < 0.05$, Fig. 6*F*), with the splenic signal being the most notable.

Discussion

In multicellular organisms, cell–cell communication plays an essential role in how cells interact with their environment to perform functions. Cell-based cancer immunotherapies like TILs, TCR-T cells, and CAR-T cells rely on the engagement of innate or exogenous receptors to specific antigens to induce cancer killing. Reliable tools for visualizing these interactions could advance our understanding of how adoptive cells behave in individual patients and allow for noninvasive tracking of cell therapies throughout the body. In this study, we describe an activatable multimodal reporter gene system to visualize direct communication between immune and cancer cells in vivo, and our results demonstrate imaging of antigen-dependent interactions between immune cells and cancer cells, notably using 3 Tesla MRI.

We first designed and engineered human T cells with an activatable reporter system composed of a CD19-directed SynNotch receptor and a suite of reporter genes for multimodal imaging. Our initial evaluation of these engineered cells produced significantly higher levels of luciferase in tumors bearing the targeted antigen with minimal off-target activity (Fig. 3B). We then sought to visualize this effect using MRI due to its clinical relevance and ability to generate images with high resolution and anatomical information, providing the unique ability to accurately identify reporter-expressing T cells spatially within tumors. We observed regions of significant enhancement post-contrast in CD19+ tumors, whereas CD19– tumors did not show such enhancement (Fig. 4A). Moreover, we were able to model and quantify enhanced foci within the tumors and observed similar patterns of enhancement between MRI and histology, owing to the superior resolution and three-dimensional nature of MRI compared to BLI (Fig. 5A). Additionally, we studied the dynamics of reporter activation in our system, observing peak reporter expression at 24 to 36 h post-injection of T cells into CD19+ tumors (Figs. 2A and 3). Contrastingly, another study detected prolonged expression of SynNotch-driven CAR and luciferase in mice post-intravenous injection of T cells (44). One possible contributor to this difference is varied T cell persistence within tumors after intratumoral versus intravenous delivery (45). Moreover, intratumoral delivery may encourage immediate activation of the SynNotch system in antigen-expressing tumors, whereas systemically administered T cells must first traffic to the tumor, leading to gradual and sustained reporter expression (46). It could be beneficial to elucidate the rate of replenishment of new SynNotch receptors at the cell surface, and whether intratumoral delivery causes proteolytic cleavage of SynNotch receptors at a rate which outpaces replenishment.

Building on our work in a human T cell line, we also demonstrate the adaption of our SynNotch imaging system for human NK-92 cells, a more clinically relevant immune cell. As a potential source for cell-based cancer immunotherapies, NK cells present several advantages over T cell including reduced risk for toxicities like graft-versus-host disease and cytokine release syndrome, possessing mechanisms to eliminate cancers independent of genetic modifications, and low alloreactivity that increases the feasibility for "off-the-shelf" cell products (47). In recent years, the human NK-92 cell line, alone or as CAR-NK cells, has already been used in patients with advanced blood cancers with minimal adverse effects (41, 42). Engineering NK-92 cells with our SynNotch imaging system, we observed CD19-dependent reporter expression in a subcutaneous tumor model, albeit both BLI and MRI signal were lower than signal observed from T cells (Fig. 6 A–C). We surmise this may be due to our T cells being engineered to have a higher copy number of each component compared to our

NK cells or epigenetic effects caused by where each component integrated in the genome. Interestingly, equipping NK cells with a CD19-targeting SynNotch improved their killing against CD19+ cancer cells compared to naïve NKs (SI Appendix, Fig. S5), even though SynNotch did not drive expression of therapeutic genes. Akin to other targeting strategies like bispecific or trispecific killer cell engagers (48), these preliminary results suggest that SynNotch receptors could be an alternate targeting approach to boost tumor killing by NK cells by accelerating NK-cancer cell interactions, and we hope to investigate this further. We then evaluated intravenous delivery of engineered NK cells and observed significantly higher luciferase signal in systemic tumor-bearing mice than healthy mice (Fig. 6 D–F), specifically in the liver, lungs, lower limbs, and most notably, the spleen. This pattern is consistent with the distribution of systemically injected Nalm6 and cancer-targeting NK-92 cells in mice in other studies (49, 50). However, BLI signal was still several orders of magnitude lower than in subcutaneous tumors, limiting MRI detection. We posit that adequate MR contrast would result from regional homing, expansion, and persistence of systemically delivered cells—a limitation of using NK-92 cells, which lack proliferation in animals due to irradiation prior to injection. Recent studies have emphasized an improvement in tumor infiltration, persistence, and expansion of infused cells when driving interleukin-2 (51) or a CAR upon SynNotch activation, which can both induce cell proliferation (32). We hope to incorporate similar strategies in the next iteration of our system with primary immune cells to boost activated cell detection sensitivity upon intravenous injection.

Driving MRI contrast enhancement in our cells is expression of OATP1B3, which has been previously showcased as a sensitive MRI reporter for tracking cancer cells (18, 19). The non-specific transport capabilities of OATP1B3, and its rat analog OATP1A1, have also been explored for other modalities such as fluorescence (18), single photo emission computed tomography (15), and photoacoustic imaging (52), with novel paramagnetic MRI probes for this transporter currently being developed (53). While immune cell tracking using MRI presents some notable clinical advantages, such as being completely non-ionizing and more widely distributed within the healthcare system, imaging cells with PET presents sensitivity benefits. Several PET reporters have been used for longitudinal tracking of T cells in vivo (14, 54), with some already being tested in patients (55). Recently, promising work highlighted a synthetic biology system utilizing the human simplex virus 1 thymidine kinase (HSV1-TK) for the sensitive, antigen-dependent detection of T cells using PET (56). An important advantage of OATP1B3 is its human origin and the accompanying clinically approved Gd-EOB-DTPA agent, making this reporter system highly compatible in humans by minimizing the potential risk for causing immunogenic reactions compared to HSV1-TK. Our group has previously described combining OATP1B3 for MRI with the human sodium iodine symporter for PET to track stem cells (57), and we envision our SynNotch system could incorporate these two human reporters to harness the combined strength of both clinical modalities.

A variety of synthetic receptors have been developed which allow cells to sense both soluble and membrane-bound molecules in their environment, then respond with user-defined transcriptional programs (58). In this study, we chose to employ the SynNotch system due to its high modularity and its simple signal transduction mechanism that is completely orthogonal to endogenous pathways (28). SynNotch generally relies on the presence of membrane-bound antigens which is suited for our goal of spatially tracking cell–cell communication within tumors. Arguably the greatest advantage of SynNotch compared to other systems is the ability to easily

customize both the extracellular recognition and intracellular effector domains. SynNotch receptors have been targeted against a plethora of cancer surface proteins (29, 32–34, 36) and even cancer-associated processes like angiogenesis (59). Here, we directed SynNotch against the B cell marker CD19 as an initial proof-of-concept of this system for imaging in small animals due to the clinical success of CD19-targeted immunotherapies (38). We next intend on targeting cancer antigens which are exclusive to cancers, but not healthy cells, and have higher expression levels across multiple solid tumor types. A key challenge in targeting solid tumors in the clinic remains the heterogeneity of cancer antigens (60), and this may be addressed by using multiple orthogonal SynNotch systems to create logic AND/OR gates which recognize several distinct cancer antigens to drive reporter expression (28, 61). Moreover, mechanical forces between antigen-expressing and receptor-expressing cells have been shown to facilitate Notch signaling by exposing proteolytic cleavage sites in the regulatory core (62).

The work performed here also suggests several opportunities for refinement. Although MRI did not reveal obvious regions of contrast enhancement in CD19– tumors, we did detect low levels of luciferase via BLI, which is more sensitive, indicating some leakiness of reporter expression consistent with previous studies (Fig. 3) (28). To increase the specificity of this system, an "enhanced" SynNotch receptor has been described which adds a short intracellular hydrophobic sequence to the transmembrane domain (63). These enhanced receptors exhibited reduced antigen-independent activation compared to normal SynNotch without affecting the efficiency of antigen-dependent activation. Moreover, due to the mouse Notch1 core, yeast GAL4, and herpesvirus VP64, there are some concerns with immunogenicity caused by non-human components of SynNotch. Redesigned proteolytic receptors with humanized sequences and a smaller size may be an attractive alternative to SynNotch moving forward for clinical translation (64). To better navigate clinical translation, improving the engineering of our immune cells with concise receptor and RE inserts will be critical to improve the efficiency of reporter gene activation we detected in vitro and increasing the overall detection sensitivity with MRI. In this study, the RE encoded three reporter genes for FLI, BLI, and MRI, resulting in large lentiviral transfer plasmids (>14 kb) that will limit viral titers (65). Including only a single transgene, such as OATP1B3, in the RE would greatly reduce the size of this construct, increasing viral titers for improved engineering efficiency, and even potentially facilitating an all-in-one lentiviral construct encoding both SynNotch receptor and RE to transduce cells in one step rather than serially (66). Beyond cell engineering, the vast majority of SynNotch studies thus far have driven receptor expression using the phosphoglycerate kinase promoter (pPGK), which has been shown to be weaker than promoters like human elongation factor-1 alpha (pEF1α) (67). Therefore, optimizing the expression of SynNotch receptors at the cell surface may improve reporter expression. Another factor to optimize is the activation efficiency of genes once receptors do bind. For example, this could involve tweaking the GAL4-VP64 by altering the number of DNA-binding domains within the RE (68), or exploring different transactivation systems that are human-derived and should be less immunogenic (64). While the doses of Gd-EOB-DTPA we used in this study (1.5 mmol/kg) were well within tolerance for mice (69), these doses are considerably higher relative to recommended clinical dosages (0.025 mmol/kg), although doses as high as 0.5 mmol/kg have been used in humans (70). Overall, optimizing OATP1B3 expression from our system would permit greater per cell sensitivity at the current dose, which may allow less contrast agent to be used going forward.

We predict that the ability to accurately visualize when and where cells encounter their intended targets throughout the body via MRI would be highly valuable in the development and monitoring of novel cell therapies. With further refinement, the activatable imaging system described here could be leveraged to better understand why certain cell-based immunotherapies fail in some patients, aid in strategies to overcome current barriers in targeting solid tumors, and to noninvasively monitor therapies which alter the milieu of the tumor environment to improve immune cell trafficking (71). Beyond cell therapies entirely, we envision this system could be broadly applicable as a powerful tool for preclinical research. Equipping cells with a system that allows for whole-body, tomographic visualization of cell–cell communication could be used to noninvasively interrogate how cells behave during development, normal physiology, and pathogenesis of countless diseases.

Materials and Methods

Construct Design and Lentiviral Production. To generate the lentiviral RE construct, a lentiviral vector containing the GAL4-VP64 inducible upstream activator sequence (UAS), consisting of five copies of the GAL4 DNA-binding domain sequence 5′ to a minimal CMV promoter, was acquired from Addgene as a gift from Dr. Wendell Lim (pHR_5× GAL4_UAS, #79119). The trimodal reporter gene cassette containing tdTomato (tdT), firefly luciferase (FLuc), and organic anion transporting polypeptide 1B3 (OATP1B3) genes separated by P2A and E2A self-cleaving peptides was obtained from in-house plasmids and was cloned into the base vector downstream of the UAS by Genscript. A constitutively expressed tag blue fluorescence protein (BFP) driven by the phosphoglycerate kinase promoter (pPGK) was inserted further downstream of the reporter cassette via the In-Fusion HD cloning kit (TakaraBio). The lentiviral construct encoding anti-CD19 SynNotch receptor driven by pPGK was also acquired from Addgene as a gift from Dr. Wendell Lim (pHR_PGK_antiCD19_SynNotch_Gal4VP64, #79125). Briefly, this SynNotch receptor consists of a CD19-binding single chain variable fragment fused to the mouse Notch1 regulatory core and GAL4-VP64 and also contains an N-terminal CD8α signal sequence for membrane targeting and a Myc-tag for surface staining. To produce lentivirus containing either RE (encoding inducible reporter genes) or anti-CD19 SynNotch, respective lentiviral transfer vectors, second-generation packaging plasmids (pCMV_delta_R8.2, #12263), and envelope (pMD2.G, #12259) plasmids from Addgene as gifts from Dr. Didier Trono were co-transfected into human embryonic kidney (HEK 293T) cells using Lipofectamine 3000 according to the manufacturer's instructions (ThermoFisher). Cell supernatant containing lentivirus was collected at 24 and 48 h, filtered through a 0.45 μm filter, concentrated using a Lenti-X Concentrator (TakaraBio), and stored at −80 °C prior to transduction.

Cell Culture and Engineering. Human Jurkat T cells (clone E6-1), human Nalm6 B cell lymphoblastic leukemia cells (clone G5), and human natural killer-92 (NK-92) cells (CRL-2407) were purchased from ATCC. Jurkat and Nalm6 cells were maintained in Roswell Park Memorial Institute 1640 medium (Wisent Bioproducts) supplemented with 10% (v/v) Fetal Bovine Serum (FBS) and 5% (v/v) Antibiotic-Antimycotic. NK-92 cells were maintained in Minimum Essential Medium Alpha (ThermoFisher) with 1.5 g/L sodium bicarbonate, 36 mg/L Myo-inositol, and 8.8 mg/L folic acid added. This basal media was further supplemented with 12.5% (v/v) FBS, 12.5% (v/v) Horse Serum, 0.1 mM 2-mercaptoethanol, and 500 U/mL recombinant human interleukin-2. All cells were cultured at 37 °C in 5% CO_2. The absence of mycoplasma contamination in cell cultures was routinely verified using the MycoAlert Mycoplasma Detection Kit (Lonza). To engineer T cells, naïve Jurkat cells were first transduced with lentivirus containing the inducible RE with 8 μg/mL polybrene for 6 h. Transduced cells were washed, then cells expressing BFP, deemed "RE only" cells, were sorted using a FACSAria III fluorescence-activated cell sorter (BD Biosciences). RE only cells were then sequentially transduced with the anti-CD19 SynNotch lentivirus with 8 μg/mL polybrene for 6 h. Transduced cells were washed, stained with an anti-Myc antibody (#2233S, NEB), then Myc and BFP-positive cells were sorted to obtain "SynNotch+RE" cells. To boost the copy number of each transgene component within the cells, we performed a second round of transduction with both RE and SynNotch lentivirus in the same order followed by sorting. Naïve NK-92 cells were

transduced using an identical approach to generate RE only and SynNotch+RE NK cells. Expression of each component in cells was validated post-sort by performing flow cytometry on a FACSCanto (BD Biosciences). All flow cytometry results were analyzed using FlowJo v10 software (FlowJo LLC, BD Biosciences). To engineer Nalm6 cells that can be tracked using BLI, naïve CD19+ Nalm6 cells were transduced using human elongation factor-1 alpha promoter (pEF1α)-driven lentiviral vectors encoding zsGreen (zsG) and Antares reporter (72), and zsG+ cells were sorted to purify "Nalm6 zsG Antares" cells. To generate CD19− Nalm6 cells, a Gene Knockout Kit v2 from Synthego was used according to the manufacturer's instructions. Briefly, sgRNA against human CD19 and Cas9-2NLS were mixed at a 6:1 ratio, then incubated for 10 min at room temperature to form the ribonucleoprotein (RNP) complex. One million naïve Nalm6 cells were resuspended in 100 µL 4D-Nucleofector solution, mixed with RNP complex, and nucleofected using program CV-104 on the 4D-Nucleofector X unit (Lonza). Following nucleofection, cells were resuspended with pre-warmed medium and transferred to 96-well plate. Five days post-nucleofection, CD19− cells were sorted and flow cytometry was performed to validate knockout of CD19 using a fluorescently tagged CD19 antibody (#302220, Biolegend). To detect surface markers, T cells were stained for human T cell receptor (TCR, #306720), CD3 (#317335), CD4 (#357409), and CD8 (#300912) using fluorescently tagged antibodies (Biolegend), and flow cytometry was performed to assess percentage of cells expressing each molecule. Cell proliferation was measured using a tetrazolium salt 3-(4,5-dimethylthiazol-2-yl)-2,5 diphenyltetrazolium bromide (MTT) Assay Kit according to the manufacturer's instructions (#ab211091, Abcam). MTT assays were performed on cells immediately following seeding 10^5 cells into 96-well plates and at 24 and 48 h post-seeding. Relative growth rates were calculated by normalizing absorbance measurements at 24 and 48 h to absorbance values obtained at seeding.

In Vitro Experiments. For in vitro experiments, Jurkat T cell populations were co-cultured with CD19+ or CD19− Nalm6 cells. For a 1:1 ratio, 10^5 of each cell type was used. For varying target cell numbers, 10^5 T cells were used while the number of Nalm6 target cells was varied. For bioluminescence imaging (BLI) and flow cytometry, cells were mixed in a 96-well round bottom plate, whereas for microscopy, a 96-well flat bottom plate was used. After seeding the cell types in wells, plates were centrifuged at 400 g for 5 min to improve the interaction between cell types. For BLI, 150 µg/mL D-luciferin (Syd Lab) was added to each well and plates were immediately imaged on an IVIS Lumina XRMS scanner (PerkinElmer). Average radiance (p/s/cm²/sr) per well was quantified by placing regions-on-interest over each well using Living Image 4.5.2 software (PerkinElmer). To evaluate the percentage of tdT+ T cells, the percentage of BFP+ cells (from RE element) that were also tdT+ was evaluated via flow cytometry. To generate time-lapse movies, co-cultured cells were imaged using the CytoSMART Lux3 FL incubator microscope (CytoSMART Technologies BV). Brightfield (exposure: 9 ms) and tdT (exposure: 1,300ms; gain: 45, intensity: 90%) images were acquired immediately after mixing cells every 10 min for up to 40 h. Counts of tdT+ cells in microscopy images were obtained from CytoSMART software via the object count algorithm. To perform the OATP1B3 uptake assay, co-cultured T cells were collected at 24 h post-seeding and incubated with Live/Dead Fixable Green (LDG) Dye (ThermoFisher) according to the manufacturer's instructions. Cells were then co-incubated with the Sytox Red Dead Cell Stain (ThermoFisher) to stain any dead cells. The percentage of live BFP+ cells that were also LDG+ was analyzed using flow cytometry. To evaluate toxicities from our gadolinium agent, at 24 h post-seeding, an appropriate volume of Gd-EOB-DTPA (Primovist; Bayer) was added to CD19+ co-cultures to achieve the indicated concentration in media. Cells were incubated with agent for 90 min, then washed and collected, and the percentage of live BFP+ cells (Sytox Red−) was analyzed using flow cytometry.

For all NK-92 experiments, 30 min prior to use, NK cells were irradiated with 5 Gy using the CellRad X-ray irradiator by Faxitron. Co-culture experiments for NK cells were performed using an identical protocol to those with T cells. For killing assays, $5 × 10^4$ Nalm6 zsG Antares cells were seeded in each well, then the appropriate number of NK cells number was added to reflect the indicated E:T ratio. After 24 h, the percentage of live Nalm6 cells (zsG+) was determined using flow cytometry.

Animal Models. All animal procedures were performed as approved by the University Council on Animal Care at the University of Western Ontario (Protocol #2020-025) and follow the Canadian Council on Animal Care and Ontario Ministry of Agricultural, Food and Rural Affairs guidelines. For all animal work,

6 to 8-wk-old female NOD.Cg-$Prkdc^{scid}$ $Il2rg^{tm1Wjl}$/SzJ (NSG) mice were obtained from an in-house breeding colony at Western University. For our subcutaneous tumor model, CD19+ or CD19− Nalm6 cells (10^6) resuspended in 50 µL PBS was mixed with an equal volume of Matrigel (Corning) and injected subcutaneously into the right flank of each mouse. Tumor volumes were periodically monitored using manual calipers and were deemed ready once tumors reached ~150 mm³ (~3 to 5 wk postinoculation). For T cells, mice received an intratumoral injection of 10^7 SynNotch+RE T suspended in 100 µL PBS. For NK cells, mice received an intratumoral or intravenous tail vein injection of 10^7 (unless otherwise indicated) irradiated SynNotch+RE NK cells suspended in 100 µL PBS. For our systemic tumor model, $5 × 10^6$ Nalm6 zsG Antares cells in 100 µL PBS were injected via the tail vein into each mouse. At day 11 post-tumor inoculation, mice received $5 × 10^6$ irradiated SynNotch+RE NK cells in 100 µL PBS via the tail vein.

In Vivo and Ex Vivo BLI. BLI on mice was performed using the IVIS Lumina XRMS scanner (PerkinElmer) 24 h prior to immune cell injection and then at indicated time point post-cell injection. Mice were anesthetized and maintained using 2% isoflurane in oxygen using a nose cone attached to an activated carbon filter for passive scavenging and kept warm on a heated stage. Mice subsequently received an intraperitoneal injection of 100 mg/kg D-luciferin for FLuc or 25 µL Fluoro-furimazine (Promega) for Antares. Bioluminescence images were captured using an automatic exposure time (max. 60 s) until peak signal was reached (~10 to 30 min per mouse). For subcutaneous tumors, average radiance (p/s/cm²/sr) was quantified by placing regions-on-interest (ROIs) over the primary tumor using Living Image 4.5.2 software (PerkinElmer). For systemic cancer models, average radiance was quantified by placing ROIs over the entire animal to measure tumor burden, or over the indicated region. Ex vivo BLI was performed ~30 min following normal BLI on day 2 post-injection of NK cells. First, mice were euthanized with an overdose of isoflurane, then excised organs were imaged, and average radiance was quantified by drawing ROIs over each organ.

In Vivo MRI. MRI was performed on a 3 Tesla GE clinical MR scanner (General Electric Healthcare Discovery MR750 3.0T) using a custom-built gradient insert and a bespoke 5-cm-diameter birdcage radiofrequency coil as previously described (19). Throughout the scan, mice were anesthetized and maintained using 2% isoflurane in oxygen using a nose cone attached to an activated carbon filter for passive scavenging. Respiratory rate and body temperature were monitored throughout the scan, and mice were kept warm throughout. T_1-weighted images were acquired using a spoiled gradient recalled acquisition in steady state (SPGR) pulse sequence using the following parameters: FOV = 50 mm; TR = 14.7 ms; TE = 3.16 ms; receive BW = ±31.25 kHz; matrix size = 250 × 250; flip angle = 60°; NEX = 3; 200 µm isotropic voxels; scan time = ~17 min. At 24 h post-intratumoral injection of T cells, a pre-contrast image was taken and then mice were administered 1.5 mmol/kg Gd-EOB-DTPA (Primovist; Bayer) via the tail vein. To reduce the effects of non-specific uptake by tissues, post-contrast MRI was performed 5 h after Primovist administration as previously described (16). Following image acquisition, transverse slices containing tumor regions were selected in Horos Project Software (horosproject.com) and saved as an image series. With the help of a blinded observer, contrast-to-noise ratio (CNR) of post-contrast MRI images was calculated by drawing ROIs over the enhanced region(s) in Horos. In slices with no clear regions of contrast, the observer was asked to estimate a ROI on the tumor. CNR was calculated by taking the difference in mean signal intensity between drawn ROIs and non-enhanced tumor background and dividing by the SD of background signal.

$$CNR = \frac{MEAN_{ROI} - MEAN_{non-enhanced}}{STDEV_{background}}.$$

To generate intensity profiles, the line tool in in ImageJ (https://imagej.nih.gov/ij/index.html) was used to place a straight line across the midsection of each tumor and pixel gray values along the line were plotted for all transverse slices corresponding to the tumor using MATLAB (Mathworks). To count the number of bright pixels in each tumor, tumors on each slice were manually segmented using the polygon tool in ImageJ and the total number of pixels at each gray value (0 to 255) was tallied throughout each tumor. Using MATLAB, a threshold for each animal was calculated from pre-contrast images using the following equation:

$$THRESHOLD = MEAN_{pre} + A × STDEV_{pre}, \text{ where } A = 2, 3, 4, \text{ or } 5.$$

In post-contrast images for each animal, the number of pixels with values above the corresponding threshold was counted and expressed as a percentage of the total number of pixels in each tumor.

$$BRIGHT\ PIXEL\% = \frac{\sum PIXELS\ ABOVE\ THRESHOLD}{\sum TUMOUR\ PIXELS}.$$

Histology and Immunostaining. At endpoint, animals were euthanized with an overdose of isoflurane and tissues were pressure perfused via the left ventricle with 4% paraformaldehyde (PFA). Tumors were excised, submerged in 4% PFA for 24 h, and stored in PBS at 4 °C prior to sectioning and staining. Tumors were submerged through 10 to 30% sucrose gradients, then frozen in optimal cutting temperature medium (Sakura Finetek), and 10 μm frozen sections were cut. Frozen tumor sections were fixed in 4% paraformaldehyde (PFA) for 10 min at room temperature and then stained with hematoxylin and eosin (H&E), DAPI, or anti-OATP1B3 antibody (HPA004943, Sigma-Aldrich). All fluorescence images were captured on an EVOS FL Auto 2 (ThermoFisher).

Statistics. All statistical analyses were performed in GraphPad Prism 9.0 software (GraphPad Software Inc.). For in vitro BLI, cell proliferation, and killing assays, a two-way ANOVA followed by Tukey's multiple comparisons test was used. For surface marker staining and Primovist incubations, a one-way ANOVA followed by Tukey's multiple comparisons test was used. For in vivo BLI, a repeated measures two-way ANOVA followed by Sidak's multiple comparisons test was used. For BLI and MRI quantification between two groups, an unpaired t test was used to measure differences between groups. Welch's and Geisser-Greenhouse corrections were used for appropriate tests. For all tests, a nominal P-value less than 0.05 was deemed significant.

Data, Materials, and Software Availability. All study data are included in the article and/or *SI Appendix*. MRI analysis tools and scripts used to generate intensity profiles and count bright pixels are available at https://github.com/twang342/MRI-Analysis-Tools.

Author affiliations: [a]Department of Medical Biophysics, Schulich School of Medicine & Dentistry, Western University, London, ON N6A 3K7, Canada; [b]Imaging Laboratories, Robarts Research Institute, London, ON N6A 5B7, Canada; [c]Ontario Institute of Cancer Research, Toronto, ON M5G 0A3, Canada; [d]Department of Microbiology and Immunology, Schulich School of Medicine & Dentistry, Western University, London, ON N6A 3K7, Canada; [e]Department of Oncology, Division of Experimental Oncology, Schulich School of Medicine & Dentistry, Western University, London, ON N6A 3K7, Canada; and [f]Lawson Health Research Institute, London, ON N6C 2R5, Canada

1. E. W. Weber, M. V. Maus, C. L. Mackall, The emerging landscape of immune cell therapies. *Cell* **181**, 46–62 (2020).
2. N. P. Staff, D. T. Jones, W. Singer, Mesenchymal stromal cell therapies for neurodegenerative diseases. *Mayo Clin. Proc.* **94**, 892–905 (2019).
3. D. L. Porter, B. L. Levine, M. Kalos, A. Bagg, C. H. June, Chimeric antigen receptor-modified T cells in chronic lymphoid leukemia. *N. Engl J. Med.* **365**, 725–733 (2011).
4. S. L. Maude *et al.*, Chimeric antigen receptor T cells for sustained remissions in leukemia. *N. Engl J. Med.* **371**, 1507–1517 (2014).
5. M. Sadelain, I. Riviere, R. Brentjens, Targeting tumours with genetically enhanced T lymphocytes. *Nat. Rev. Cancer* **3**, 35–45 (2003).
6. A. Grakoui *et al.*, The immunological synapse: A molecular machine controlling T cell activation. *Science* **285**, 221–227 (1999).
7. J. B. Huppa, M. M. Davis, T-cell-antigen recognition and the immunological synapse. *Nat. Rev. Immunol.* **3**, 973–983 (2003).
8. O. Penack, C. Koenecke, Complications after CD19 + CAR T-Cell Therapy. *Cancers* **12**, 1–17 (2020).
9. J.-X. Cao *et al.*, The efficacy of anti-CD19 chimeric antigen receptor T cells for B-cell malignancies. *Cytotherapy* **21**, 769–781 (2019).
10. A. G. Selim *et al.*, CAR-T cell therapy: Practical guide to routine laboratory monitoring. *Pathology (Phila.)* **53**, 408–415 (2021).
11. E. T. Ahrens, J. W. Bulte, Tracking immune cells in vivo using magnetic resonance imaging. *Nat. Rev. Immunol.* **13**, 755–763 (2013).
12. J. H. Kang, J.-K. Chung, Molecular-genetic imaging based on reporter gene expression. *J. Nucl. Med.* **49**, 164S–179S (2008).
13. N. Shalaby, V. P. Dubois, J. Ronald, Molecular imaging of cellular immunotherapies in experimental and therapeutic settings. *Cancer Immunol. Immunother* **71**, 1–14 (2021).
14. C. Ashmore-Harris, M. Iafrate, A. Saleem, G. O. Fruhwirth, Non-invasive reporter gene imaging of cell therapies, including T cells and stem cells. *Mol. Ther.* **28**, 1392–1416 (2020).
15. P. S. Patrick *et al.*, Dual-modality gene reporter for in vivo imaging. *Proc. Natl. Acad. Sci. U.S.A.* **111**, 415–420 (2014).
16. N. N. Nystrom *et al.*, Longitudinal visualization of viable cancer cell intratumoral distribution in mouse models using Oatp1a1-enhanced magnetic resonance imaging. *Invest. Radiol.* **54**, 302–311 (2019).
17. M. Narita *et al.*, Expression of OATP1B3 determines uptake of Gd-EOB-DTPA in hepatocellular carcinoma. *J. Gastroenterol.* **44**, 793–798 (2009).
18. M. R. Wu *et al.*, Organic anion-transporting polypeptide 1B3 as a dual reporter gene for fluorescence and magnetic resonance imaging. *FASEB J.* **32**, 1705–1715 (2018).
19. J. J. Kelly *et al.*, Safe harbor-targeted CRISPR-Cas9 homology-independent targeted integration for multimodality reporter gene-based cell tracking. *Sci. Adv.* **7**, 1–15 (2021).
20. N. Nyström, Sensitive spatiotemporal tracking of spontaneous metastasis in deep tissues via a genetically-encoded magnetic resonance imaging reporter. BioRxiv (2022).
21. H. Daneshpour, H. Youk, Modeling cell–cell communication for immune systems across space and time. *Curr. Opin. Syst. Biol.* **18**, 44–52 (2019).
22. J. H. Jang *et al.*, Imaging of cell-cell communication in a vertical orientation reveals high-resolution structure of immunological synapse and novel PD-1 dynamics. *J. Immunol.* **195**, 1320–1330 (2015).
23. J. Rossy, S. V. Pageon, D. M. Davis, K. Gaus, Super-resolution microscopy of the immunological synapse. *Curr. Opin. Immunol.* **25**, 307–312 (2013).
24. A. Rudkouskaya *et al.*, Quantitative imaging of receptor-ligand engagement in intact live animals. *J. Control Release* **286**, 451–459 (2018).
25. M. A. Sellmyer *et al.*, Visualizing cellular interactions with a generalized proximity reporter. *Proc. Natl. Acad. Sci. U.S.A.* **110**, 8567–8572 (2013).
26. R. Kojima, M. Fussenegger, Engineering whole mammalian cells for target-cell-specific invasion/fusion. *Adv. Sci.* **5**, 1700971 (2018).
27. A. A. Gilad, M. G. Shapiro, Molecular imaging in synthetic biology, and synthetic biology in molecular imaging. *Mol. Imaging Biol.* **19**, 373–378 (2017).
28. L. Morsut *et al.*, Engineering customized cell sensing and response behaviors using synthetic notch receptors. *Cell* **164**, 780–791 (2016).
29. K. T. Roybal *et al.*, Engineering T cells with customized therapeutic response programs using synthetic notch receptors. *Cell* **167**, 419–432 (2016).
30. S. Toda *et al.*, Engineering synthetic morphogen systems that can program multicellular patterning. *Science* **370**, 327–331 (2020).
31. H. Huang *et al.*, Cell-cell contact-induced gene editing/activation in mammalian cells using a synNotch-CRISPR/Cas9 system. *Protein Cell* **11**, 299–303 (2020).
32. J. H. Choe *et al.*, SynNotch-CAR T cells overcome challenges of specificity, heterogeneity, and persistence in treating glioblastoma. *Sci. Transl. Med.* **13**, 1–16 (2021).
33. A. Hyrenius-Wittsten *et al.*, SynNotch CAR circuits enhance solid tumor recognition and promote persistent antitumor activity in mouse models. *Sci. Transl. Med.* **13**, 1–16 (2021).
34. J. H. Cho *et al.*, Engineering Axl specific CAR and SynNotch receptor for cancer therapy. *Sci. Rep.* **8**, 1–8 (2018).
35. L. He, J. Huang, N. Perrimon, Development of an optimized synthetic Notch receptor as an in vivo cell–cell contact sensor. *Proc. Natl. Acad. Sci. U.S.A.* **114**, 5467–5472 (2017).
36. B. Moghimi *et al.*, Preclinical assessment of the efficacy and specificity of GD2-B7H3 SynNotch CAR-T in metastatic neuroblastoma. *Nat. Commun.* **12**, 1–15 (2021).
37. R. H. Scheuermann, E. Racila, CD19 antigen in leukemia and lymphoma diagnosis and immunotherapy. *Leuk Lymphoma* **18**, 385–397 (1995).
38. M. Sadelain, CAR therapy: The CD19 paradigm. *J. Clin. Invest.* **125**, 3392–400 (2015).
39. K. T. Roybal *et al.*, Engineering T cells with customized therapeutic response programs using synthetic notch receptors. *Cell* **167**, 419–432.e16 (2016).
40. I. Patik *et al.*, Identification of novel cell-impermeant fluorescent substrates for testing the function and drug interaction of Organic Anion-Transporting Polypeptides, OATP1B1/1B3 and 2B1. *Sci. Rep.* **8**, 2630 (2018).
41. X. Tang *et al.*, First-in-man clinical trial of CAR NK-92 cells: Safety test of CD33-CAR NK-92 cells in patients with relapsed and refractory acute myeloid leukemia. *Am. J. Cancer Res.* **8**, 1083–1089 (2018).
42. T. Tonn *et al.*, Treatment of patients with advanced cancer with the natural killer cell line NK-92. *Cytotherapy* **15**, 1563–1570 (2013).
43. Q. Liu *et al.*, Irradiated chimeric antigen receptor engineered NK-92MI cells show effective cytotoxicity against CD19 + malignancy in a mouse model. *Cytotherapy* **22**, 552–562 (2020).
44. K. T. Roybal *et al.*, Precision tumor recognition by T cells with combinatorial antigen-sensing circuits. *Cell* **164**, 770–779 (2016).
45. P. Sridhar, F. Petrocca, Regional delivery of chimeric antigen receptor (CAR) T-cells for cancer therapy. *Cancers* **9**, 1–10 (2017).
46. R. Fu *et al.*, Delivery techniques for enhancing CAR T cell therapy against solid tumors. *Adv. Funct. Mater.* **31**, 1–17 (2021).
47. G. Xie *et al.*, CAR-NK cells: A promising cellular immunotherapy for cancer. *EBioMedicine* **59**, 1–10 (2020).
48. M. K. Gleason *et al.*, Bispecific and trispecific killer cell engagers directly activate human NK cells through CD16 signaling and induce cytotoxicity and cytokine production. *Mol. Cancer Ther.* **11**, 2674–2684 (2012).
49. X. Liu *et al.*, Improved anti-leukemia activities of adoptively transferred T cells expressing bispecific T-cell engager in mice. *Blood Cancer J.* **6**, e430 (2016).
50. H. E. Daldrup-Link *et al.*, In vivo tracking of genetically engineered, anti-HER2/neu directed natural killer cells to HER2/neu positive mammary tumors with magnetic resonance imaging. *Eur. Radiol.* **15**, 4–13 (2005).
51. G. M. Allen *et al.*, Synthetic cytokine circuits that drive T cells into immune-excluded tumors. *Science* **378**, eaba1624 (2022).
52. N. N. Nystrom, L. C. M. Yip, J. J. L. Carson, T. J. Scholl, J. A. Ronald, Development of a human photoacoustic imaging reporter gene using the clinical dye indocyanine green. *Radiol. Imaging Cancer* **1**, 1–8 (2019).
53. N. N. Nystrom *et al.*, Gadolinium-free magnetic resonance imaging of the liver using an Oatp1-targeted Manganese(III) porphyrin. *J. Med. Chem.* (2021).

54. S. S. Yaghoubi et al., Noninvasive detection of therapeutic cytolytic T cells with 18F–FHBG PET in a patient with glioma. Nat. Clin. Pract. Oncol. 6, 53–58 (2009).

55. K. V. Keu et al., Reporter gene imaging of targeted T cell immunotherapy in recurrent glioma. Sci. Transl. Med. 9, 1–10 (2017).

56. J. Shin et al., Antigen-dependent inducible T cell reporter system for PET imaging of breast cancer and glioblastoma. J. Nucl. Med. 64, 137–144 (2022).

57. N. Shalaby, A human-derived dual MRI/PET reporter gene system with high translational potential for cell tracking. Mol. Imaging Biol. 24, 341–351 (2022).

58. A. Teixeira, M. Fussenegger, Engineering mammalian cells for disease diagnosis and treatment. Curr. Opin. Biotechnol. 55, 87–94 (2019).

59. Z. Wang et al., Using apelin-based synthetic Notch receptors to detect angiogenesis and treat solid tumors. Nat. Commun. 11, 2163 (2020).

60. S. Rafiq, C. S. Hackett, R. J. Brentjens, Engineering strategies to overcome the current roadblocks in CAR T cell therapy. Nat. Rev. Clin. Oncol. 17, 147–167 (2019).

61. S. Simon, G. Bugos, A. I. Salter, S. R. Riddell, Synthetic receptors for logic gated T cell recognition and function. Curr. Opin. Immunol. 74, 9–17 (2022).

62. W. R. Gordon et al., Mechanical allostery: Evidence for a force requirement in the proteolytic activation of notch. Dev. Cell 33, 729–736 (2015).

63. Z. J. Yang, Z. Y. Yu, Y. M. Cai, R. R. Du, L. Cai, Engineering of an enhanced synthetic Notch receptor by reducing ligand-independent activation. Commun. Biol. 3, 1–7 (2020).

64. I. Zhu et al., Modular design of synthetic receptors for programmed gene regulation in cell therapies. Cell 185, 1431–1443.e16 (2022).

65. N. al Yacoub, M. Romanowska, N. Haritonova, J. Foerster, Optimized production and concentration of lentiviral vectors containing large inserts. J. Gene Med. 9, 579–584 (2007).

66. Z. Niu et al., Chimeric antigen receptor-modified macrophages trigger systemic anti-tumour immunity. J. Pathol. 253, 247–257 (2021).

67. J. Y. Qin et al., Systematic comparison of constitutive promoters and the doxycycline-inducible promoter. PLoS One 5, 1–4 (2010).

68. Y. Zhang et al., Optimization of the Gal4/UAS transgenic tools in zebrafish. Appl. Microbiol. Biotechnol. 103, 1789–1799 (2019).

69. O. Döhr, R. Hofmeister, M. Treher, H. Schweinfurth, Preclinical Safety Evaluation of Gd-EOB-DTPA (Primovist). Invest. Radiol. 42, 830–841 (2007).

70. G. Schuhmann-Giampieri, M. Mahler, G. Röll, R. Maibauer, S. Schmitz, Pharmacokinetics of the liver-specific contrast agent Gd-EOB-DTPA in relation to contrast-enhanced liver imaging in humans. J. Clin. Pharmacol. 37, 587–596 (1997).

71. A. J. Hou, L. C. Chen, Y. Y. Chen, Navigating CAR-T cells through the solid-tumour microenvironment. Nat. Rev. Drug Discov. 20, 531–550 (2021).

72. J. Chu et al., A bright cyan-excitable orange fluorescent protein facilitates dual-emission microscopy and enhances bioluminescence imaging in vivo. Nat. Biotechnol. 34, 760–767 (2016).